

PACS numbers: 78.40.-q, 79.20.Eb, 87.64.Cc, 87.64.Ee, 87.19.xb, 87.50.W-, 87.85.Rs

## Characterization and Evaluation of the Antimicrobial Activity of CuO Nanoparticles Prepared by Pulse Laser Ablation in Double-Distilled Water

Khalaf Ajaj, Abdullah M. Ali, and Mushtaq Abed Al-Jubbori

*College of Education for Pure Sciences,  
Department of Physics,  
University of Tikrit,  
41001 Mosul, Iraq*

In the current research, Q-switched Nd:YAG-laser ablation is used to create the copper-oxide nanoparticles (NPs). A disc-shaped copper target is subjected to the ablation procedure, while it is submerged in double-distilled water. The ablation is carried out with pulse counts ranging from 100, 200, 300, 400, and 500 with two different energy levels, namely, 200 mJ and 400 mJ. Transmission electron microscopy (TEM), x-ray diffraction analysis (XRD), and UV-vis spectrophotometry are used to determine the morphological and optical properties of nanoparticles. An increase in the absorbance spectrum with an increase in the number of pulses indicates an increase in the concentration of copper-oxide nanoparticles. The peaks of surface-plasmon resonance at 217 nm are seen in the absorption spectra as the laser pulses increased. A slight reduction in the optical band gap is occurred too. CuO-NPs' formation is verified by XRD analysis, which also reveals that the copper-oxide NPs' structure is a monoclinic lattice. Further, the results of the TEM and UV-vis analyses show that there are presented CuO nanoparticles. CuO nanoparticles, which are nearly spherical, are found, according to the findings of the TEM and UV-vis analyses. When 200 mJ and 400 mJ of energy are used, it is discovered that the average diameters of these nanoparticles are of about 46 nm and 52 nm, respectively. Additionally, our study results show that CuO NPs at 200 mJ are more effective for inhibiting *S. aureus* and *E. coli* than they are at 400 mJ with the same number of pulses.

У поточному дослідженні абляція лазером Nd:YAG із модуляцією добротності використовували для створення наночастинок оксиду Купруму. Дискподібну мідну мішень піддавали процедурі абляції, занурюючи її у двічі дистильовану воду. Абляцію проводили з підрахунком імпульсів у діапазоні від 100, 200, 300, 400 і 500 з двома різними рівнями енергії, а саме, 200 мДж і 400 мДж. Для визначення морфологіч-

них та оптичних властивостей наночастинок використовували просвітлювальну електронну мікроскопію (ПЕМ), рентгенівську дифракційну аналізу (РДА) та спектрофотометричну аналізу у видимій та ультрафіолетовій областях світла. Збільшення спектру поглинання зі збільшенням кількості імпульсів свідчить про збільшення концентрації наночастинок оксиду Купруму. Піки поверхневого плазмонного резонансу біля 217 нм були помітні в спектрах поглинання, коли лазерні імпульси збільшувалися. Також відбулося незначне зменшення оптичної забороненої смуги. Утворення CuO-наночастинок було підтверджено РДА, яка також показала, що структура наночастинок оксиду Купруму була моноклінною ґратницею. Крім того, результати ПЕМ та спектрофотометричної аналізи показали наявність наночастинок CuO. Наночастинки CuO, які були майже сферичними, було знайдено згідно з результатами ПЕМ і спектрофотометричної аналізи. Коли було використано рівні енергії у 200 мДж і 400 мДж, було виявлено, що середні діаметри цих наночастинок становили приблизно 46 нм і 52 нм відповідно. Крім того, результати нашого дослідження показують, що CuO-наночастинки за умови 200 мДж були ефективнішими для інгібування *S. aureus* і *E. coli*, ніж за умови рівня 400 мДж з такою ж кількістю імпульсів.

**Key words:** copper-oxide nanoparticles, UV-visible laser ablation, XRD, TEM, particle size, antibacterial activity.

**Ключові слова:** наночастинки оксиду Купруму, УФ-видима лазерна абляція, РДА, ПЕМ, розмір частинок, антибактеріальна активність.

(Received 18 May, 2023; in revised form, 27 May, 2023)

## 1. INTRODUCTION

The nanoparticles (NPs) offer significant scientific benefits as they serve as a crucial intermediary between macroscopic materials and atomic or molecular structures. The physical properties of bulk materials are required to remain constant and independent of size, while at the nanoscale, the physical properties of nanomaterials exhibit size-dependent characteristics, such as quantum size effect and quantum confinement in semiconductor nanoparticles, as well as surface plasmon resonance in certain metal nanoparticles [1]. The optimal methods for synthesizing metallic nanoparticles should exhibit reproducibility and the capacity to regulate particle shape while achieving uniform yields. In addition, the method exceptional qualities include the exclusion of toxic precursors, utilization of eco-friendly solvents, maintenance of reaction temperature in proximity to ambient temperature, and reduction of by-product production [2].

Pulse laser ablation in liquid (PLAL) presents distinct advantages for the synthesis of nanostructured particles, such as high purity, simplicity, rapidity, and the absence of the need for sophisticated

vacuum equipment or chemicals, which may contaminate the final product and pollute the environment [3, 4]. The PLAL technique, despite its experimental simplicity, is distinguished by intricate and rapid mechanisms that can be succinctly described as a series of four phases. Upon impact with a solid target, the foremost portion of the laser pulse causes the evaporation of a slender stratum of substance, thereby instigating the creation of plasma. The plasma generated at the outset gives rise to a region of elevated optical absorption, which subsequently absorbs the remainder of the laser pulse and undergoes ionization to attain a state of high pressure. The isotropic propagation of a shock wave into the surrounding medium is driven by the expansion of high-pressure plasma [5]. Throughout the duration of the laser pulse, the plasma undergoes growth and consistently accompanies and reinforces the expansion of the shock. Subsequent to the cessation of the laser pulse, the shock wave propagates outward by utilizing the internal energy present within the shock front; the decay process occurs rapidly and results in the generation of an acoustic wave within a few 100 ns [6].

The transfer of energy from plasma to liquid results in the generation of a slender gaseous envelope encircling the plasma, thereby initiating the formation of a cavitation bubble. The elevated internal pressure of the bubble propels it to expand externally. Because of the fluid mass inertia, the bubble surpasses its state of equilibrium and attains its utmost radius at the point where the temperature of the bubbles' interior matches that of the adjacent liquid [7, 8]. Upon reaching a certain stage, the vapour pressure within the bubble decreases to the saturation pressure corresponding to the temperature of the liquid, which is approximately one hundred times less than the hydrostatic pressure [9, 10].

Following this, the bubble undergoes contraction, and the inward movement persists until the gas reaches a level of compression that is sufficient to cause a reversal of the motion. Upon rebound, the bubble releases surplus energy in the form of a secondary shock. The ejected matter is usually captured by the bubble and eventually delivered into the water after the bubble collapses. This provides a relatively straightforward and feasible method for creating nanoparticles with desirable structures and properties [11–13]. Furthermore, the mechanism of nanostructuring surface is contingent upon various laser parameters, including limited to the number of laser pulses, energy per pulse, pulse width, and wavelength, as well as ambient conditions. The technique high level of confinement of plasma pressure, precise and efficient cooling and ease of use render it highly advantageous and valuable. The successful application of this technique is of significant importance in the production of oxides that are synthesized through chemical reactions occurring at

the liquid–solid interface [14, 15].

It's also through various physical parameters of laser radiation, including laser pulse energy, repetition rates, laser wavelength, focal spot size, and focusing conditions, that efficient NPs size control can be achieved [16, 17]. PLAL is used to create a variety of novel materials, including nanodiamond and related nanocrystals, metallic nanocrystals, nanocrystal alloys, and metal oxides [18, 19]. The PLAL present methodology exhibits several benefits in comparison to alternative techniques, such as its straightforwardness, lack of by-products, absence of post-synthesis washing requirements, economic feasibility, and adjustable experimental parameters. Quantum dots (QD) are a type of semiconductor nanoparticle characterized by their zero-dimensional structure. They exhibit distinct optical properties such as narrow emission peaks and a broad excitation range. The wavelengths of emission and energy gap of quantum dots are significantly influenced by the particle size, which is a result of the confinement effect [20, 21].

Copper is a widely used material due to its plentiful availability, low cost, thermal and electrical conductivity and antimicrobial characteristics. Colloidal copper-oxide nanoparticles (CuO NPs) are synthesized using pulsed laser ablation technology on a copper target in a liquid medium. CuO nanoparticles have shown potential for biomedical applications due to their antibacterial activity. Moreover, CuO nanostructured materials show utility in diverse applications, including biosensors, gas sensors, lithium-ion battery electrode materials, photo detectors, and supercapacitors [22, 23]. The phenomenon of surface plasmon resonance (SPR) is contingent upon the morphology and dimensions of the particle, in addition to the optical characteristics of the nanoparticles their distinctive, particularly their sharp plasmon absorption peak, make them highly appealing for biophysical, biochemical, and biotechnological applications [24]. Additionally, the copper oxide nanoparticles exhibited inhibitory properties against two bacterial groups, namely gram-positive bacteria such as *B. subtilis* and *S. aureus*, and gram-negative bacteria such as *E. coli* and *P. aeruginosa*. The inhibitory effects were observed to be dependent on the size of the particles [25, 26].

The present research pertains to the production of copper oxide nanoparticles through the employment of the PLAL method, where, by the manipulation of ablated energies and pulse counts, it is exercised for the purpose of control. The study examined the optical and morphological characteristics of the samples through the utilization of various analytical techniques, including UV-visible spectrophotometry, x-ray diffraction analysis, and transmission electron microscopy. Furthermore, the study employed CuO NPs to assess their antibacterial effectiveness against *Staphylococcus aureus* and *Escherichia coli*.

## 2. EXPERIMENTAL SETUP

### 2.1. Method for Preparation of CuO Nanoparticles

The colloidal solutions of CuO nanoparticles were synthesized in a liquid medium by the pulsed laser ablation technique (PLAL). A disc-shaped target made of high-purity copper (99.99%) with a diameter = 20 mm and a thickness = 2 mm was positioned 10 cm away from the laser source. The target was placed in a beaker containing 5 ml of double-distilled water (DDW).

Figure 1 illustrates the experimental setup for PLAL. The Q-switched Nd:YAG is a mechanism to generate high-intensity, short-duration pulses of light. The experimental setup employed Nd:YAG laser operating at a repetition rate of 6 Hz, emitting at a wavelength of 1064 nm and with a pulse width of 10 ns. Under standard conditions of temperature and pressure, the laser source changed two distinct energy levels 200 and 400 mJ. The number of pulses was systematically altered between 100 and 500, with increments of 100 pulses for each energy level.

Figure 2 shows the effects of laser pulses on the copper metal surface. Before to ablation, the target underwent a series of cleaning procedures involving deionized water, acetone, and ethanol to eliminate any oxide layer that may have formed due to exposure to air. Additionally, the target was subjected to ultrasonic treatment to remove any mechanical impurities. In the course of the ablation procedure, the beaker underwent a gradual rotation to prevent the formation of craters on the target surface due to the focused beam and to facilitate the dispersion of the NPs generated through the

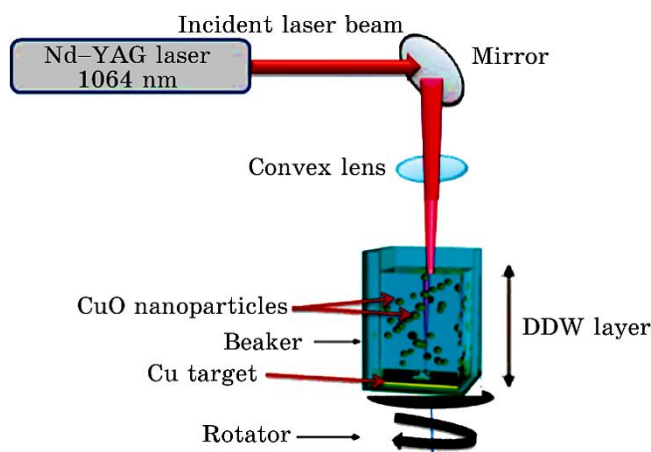


Fig. 1. PLAL system schematic diagram.

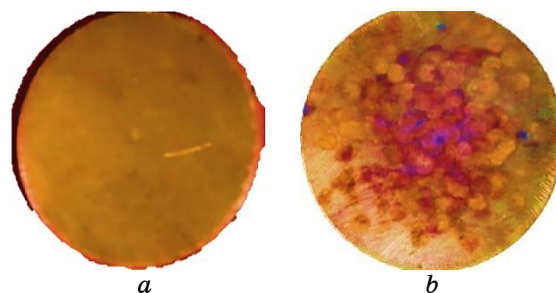


Fig. 2. Copper-metal surface ((a) before (b) after) ablated.

movement of the liquid.

## 2.2. Antibacterial Activity of CuO NPs

The medium was prepared by dissolving 37 grams of Mueller–Hinton agar (MHA) in one litre of distilled water. The pH of the medium was regulated to 7.2 and subsequently sterilized in an autoclave. Subsequently, into single-use petri dishes and positioned on a flat plane with a thickness of roughly 5 mm, followed by refrigeration at a temperature of 4 degrees Celsius until employment. The well was made in the MHA with a sterile micropipette tip. In this study, the antibacterial activity of copper-oxide nanoparticles (CuO NPs) at two different energy levels of 200 mJ and 400 mJ and with 500 pulses was evaluated using two bacterial strains, namely *Staphylococcus aureus* (gram-positive) and *Escherichia coli* (gram-negative). In this procedure, the bacteria were inoculated onto the media of the plates (MHA) using sterile cotton swabs and were evenly spread. Subsequently, a volume of 150  $\mu\text{l}$  of a colloidal solution of CuO nanoparticles was introduced to each of the previously arranged bacterial. Subsequently, the plates housing both the test organism and CuO NPs were subjected to incubation at a temperature of 37°C for duration of 24 hours. Following incubation, the impact of CuO NPs on bacterial growth was assessed through the observation of the inhibition zone and the transformation of the surface into a transparent layer, indicative of the suppression of bacterial growth.

## 3. RESULTS AND DISCUSSION

### 3.1. The Optical Properties of Copper-Oxide NPs

The investigation of spectroscopic absorption in a synthesized colloi-

dal solution of copper oxide nanoparticles in double distilled water was conducted using a Shimadzu (UV-1800) UV-vis spectrophotometer. The absorbance of colloidal nanoparticles varies with the wavelength of their absorption spectra. The findings depicted in Fig. 3 show a favourable relationship between the number of laser pulses and the level of CuO-NPs' concentration, as evidenced by the observed increase in absorption. The presence of CuO nanoparticles is indicated by the elevation of the surface-plasmon resonance peak (SPRP). Furthermore, with an increase in the number of laser pulses, the peak exhibited a reduction in width, while the dimensions of CuO NPs experienced an increase. Spherical copper oxide NPs were synthesized based on the detection of a plasmon single peak. The alteration in hue of colloidal CuO nanoparticles to a pale green, as depicted in Fig. 4, can be attributed to plasmon absorption.

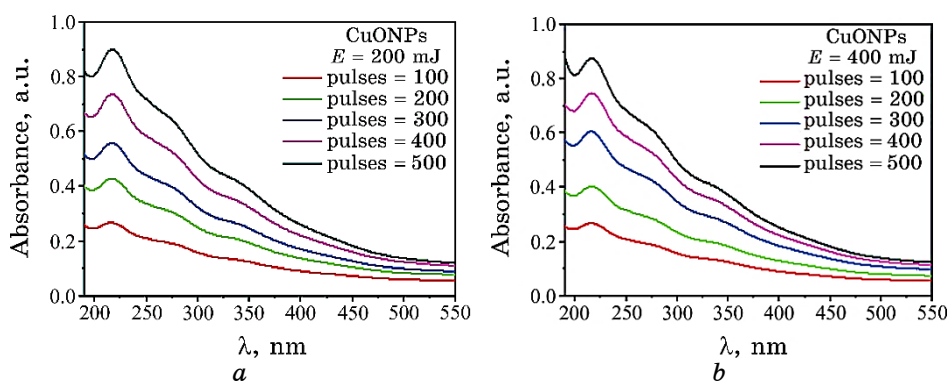


Fig. 3. Absorption spectra of CuO NPs in double distilled water at various numbers of pulses and different pulse energies.



Fig. 4. Photograph of the copper-oxide NPs prepared by PLAL using number of laser pulses and different energies (a) 200 mJ and (b) 400 mJ.

The SPRP is subject to modification by the size of the particles, resulting in a red shift towards longer wavelengths within the spectrum. Furthermore, it can be observed that the nanoparticles demonstrate a diminished absorption coefficient, resulting in elevated transmission values on the longer wavelength end of the spectrum, encompassing the visible range and wavelengths measuring up to 500 nm. The low absorption phenomenon can be elucidated by the reduction in energy of the incident photon as the wavelength increases, which results in the photon's inability to interact with the atoms present in the colloidal medium. Hence, the photons will undergo transmission instead of absorption.

The optical band gap was calculated using linear extrapolation of the equation's  $(\alpha h\nu)$  versus  $(h\nu)$  curve by fitting Tauc's relation [27]. The direct optical band gap is determined using the absorption coefficient calculated as a function of the incident photon energy. CuO nanoparticles were generated using 100 to 500 numbers of pulses at various laser energies of 200 mJ and 400 mJ:

$$(\alpha h\nu)^{1/2} = D(h\nu - E_g^{opt.}), \quad (1)$$

where  $D$  is a constant and  $h\nu$  represents the photon energy.

The absorption coefficient ( $\alpha$ ) is influenced by both the incident photon energy and the material's properties. This relationship has been utilized to calculate the absorption coefficient, which is contingent on the absorbance ( $A$ ) and the thickness ( $d$ ) [28]:

$$\alpha = \frac{2.303A}{d}. \quad (2)$$

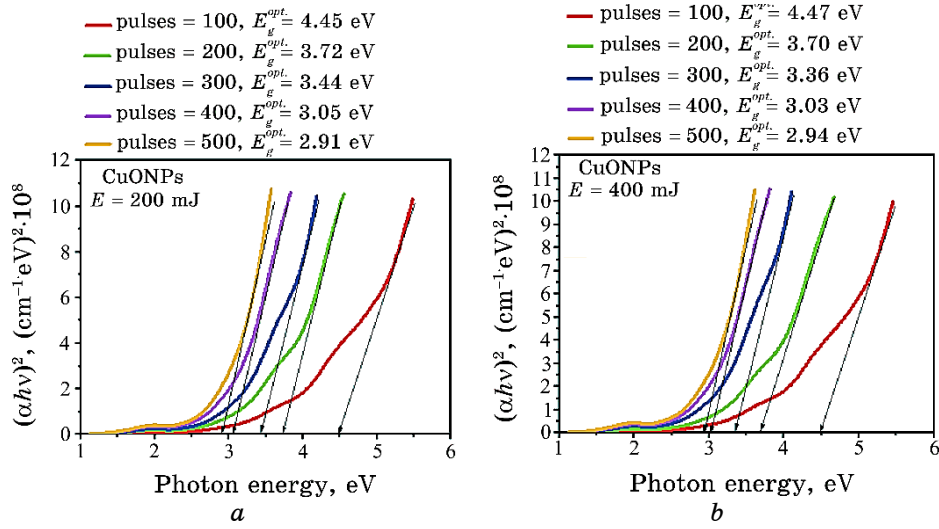
Figures 5 and 6 show the optical band gap of copper oxide nanoparticles decreased as the number of pulses has increased. This result could be due to the quantum confinement effect. This increase is a result of quantum confinement.

Figure 7 as the number of laser pulses increases, the concentration of CuO NPs causes an increase in the absorption coefficient.

From the surface-plasmon resonance peak, copper oxide nanoparticles optical constants can be evaluated their values. The refractive index ( $n$ ) is directly proportional to the concentration of CuO NPs. The refractive index can be calculated by [29, 30]:

$$n = \sqrt{\frac{4R}{(R-1)^2} - K^2} - \left(\frac{R+1}{R-1}\right), \quad (3)$$

where  $R$  and  $K$ , the reflectance and extinction coefficient, respectively. The extinction coefficient can be calculated from the relationship [31]:



**Fig. 5.** Tauc plots of the CuO NPs prepared with various laser pulse energies of (a) 200 mJ and (b) 400 mJ.

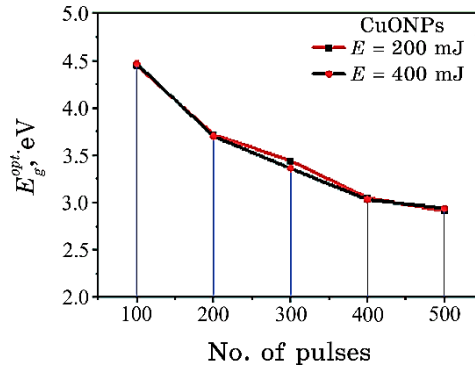


**Fig. 6.** Optical band gap values for prepared CuO NPs at various energies as a function of the number of pulses.

$$K = \frac{\alpha\lambda}{4\pi}. \quad (4)$$

The electric field of light interacts with the electrons in the nanoparticle in a way that is different from the way it interacts with electrons in bulk materials. This effect is more pronounced for smaller particles because the surface area-to-volume ratio increases as the particle size decreases. In particular, the electric field near the surface of a nanoparticle is enhanced, leading to an increase in

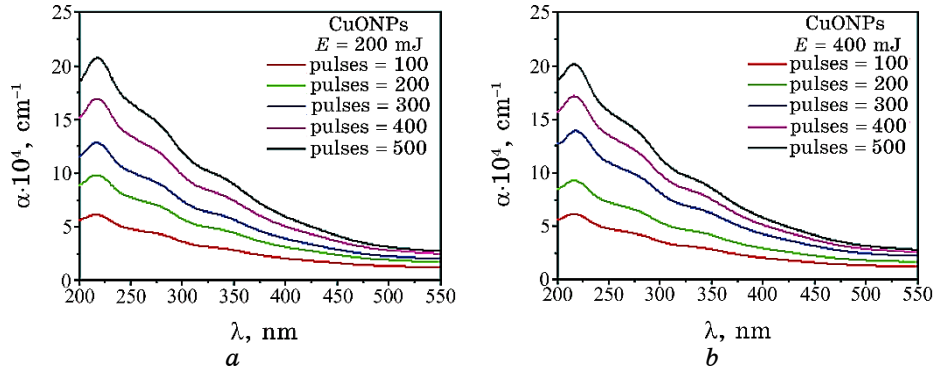


Fig. 7. Absorption coefficient *versus* wavelength of CuO NPs.

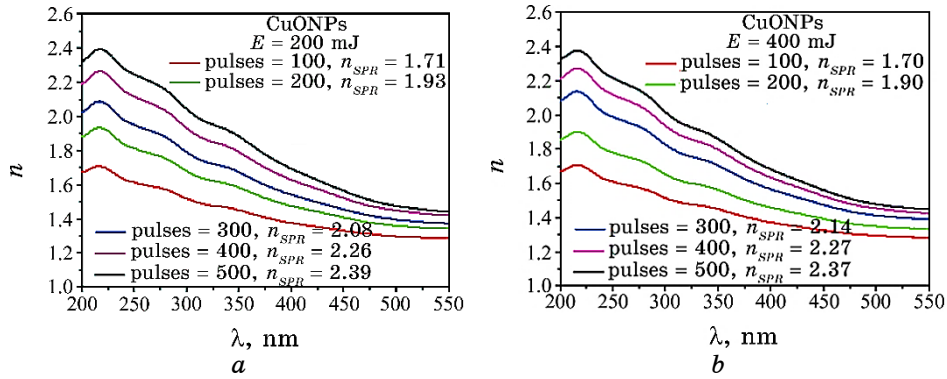


Fig. 8. Refractive index *versus* wavelength for copper-oxide NPs.

the refractive index and extinction coefficient with the number of laser pulses an increase as shown in Figs. 8 and 9.

Evaluation of the real and imaginary parts of the dielectric constant is done using the complex dielectric constant  $\varepsilon = \varepsilon_r - i\varepsilon_i = (n + iK)^2$ . The real ( $\varepsilon_r$ ) and imaginary ( $\varepsilon_i$ ) parts of the dielectric constant are related to the refractive index and extinction coefficient by the following relationships [32]:

$$\varepsilon_r = n^2 - K^2, \quad (5)$$

$$\varepsilon_i = 2nk. \quad (6)$$

Figure 10 the increase in the real and imaginary dielectric constants of copper oxide nanoparticles with increasing laser pulse number can be attributed to the enhanced polarization and increased scattering and absorption of light, respectively.

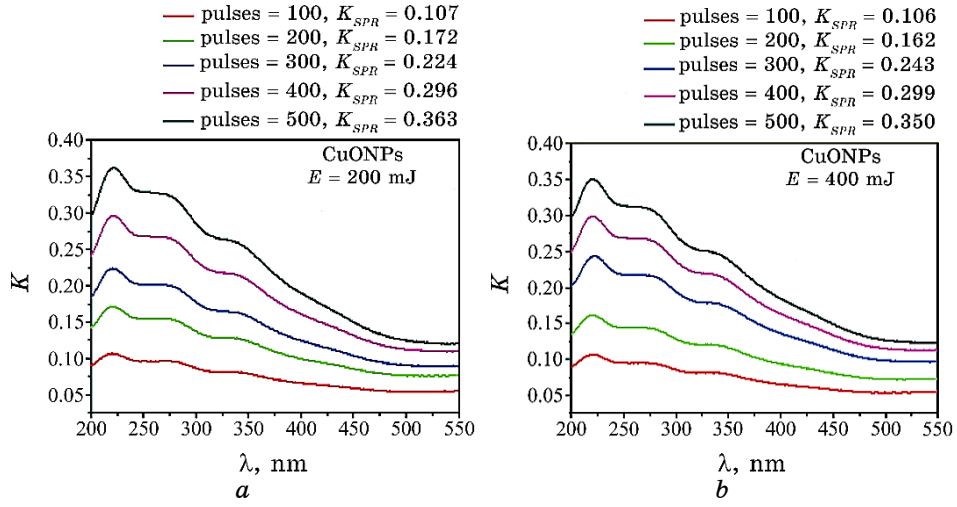


Fig. 9. Extinction coefficient *versus* wavelength for copper-oxide NPs.

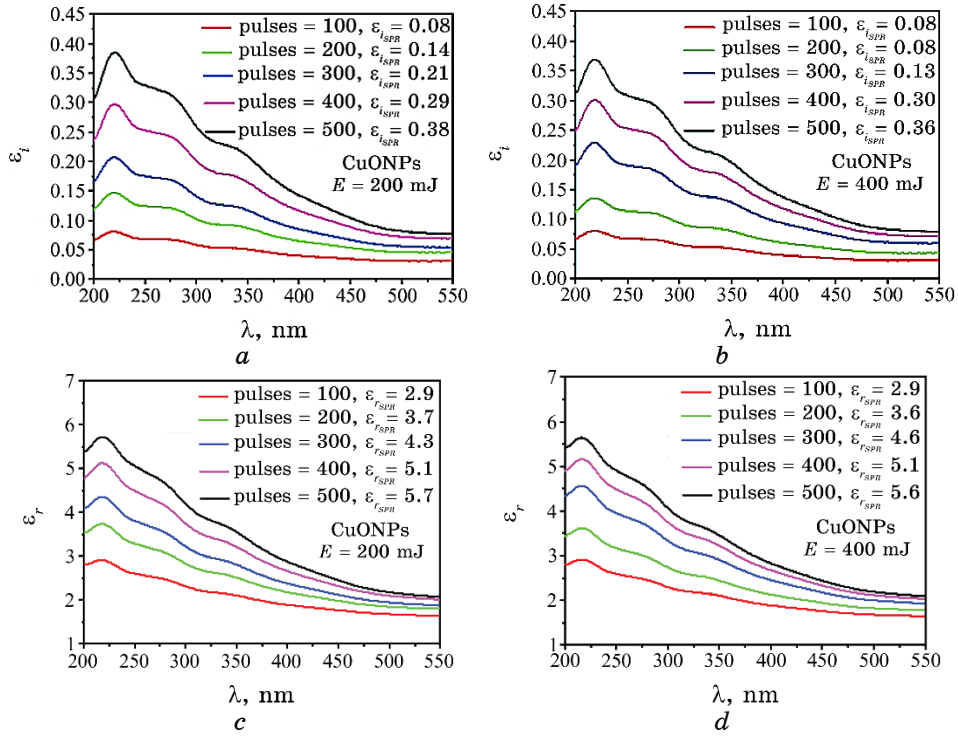
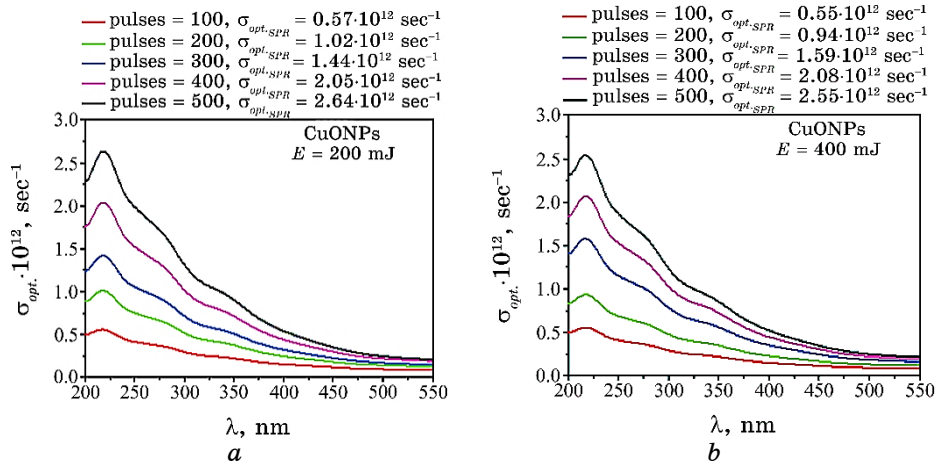


Fig. 10. Imaginary dielectric constants ((a) 200 mJ, (b) 400 mJ) and real dielectric constants ((c) 200 mJ, (d) 400 mJ) as functions of laser-pulse number.

The relationship between the linear refractive index and the linear absorption coefficient can be used to determine the optical conductivity of CuO NPs [31]:

$$\sigma_{opt.} = \frac{\alpha n c}{4\pi}, \quad (7)$$

where  $c$  is the speed of light in a vacuum. The increase in optical conductivity can be attributed to the greater number of excited electrons with increasing concentrations of CuO NPs, as shown in Fig. 11.



**Fig. 11.** Optical conductivity *versus* wavelength of CuO NPs as a function number of laser pulses.

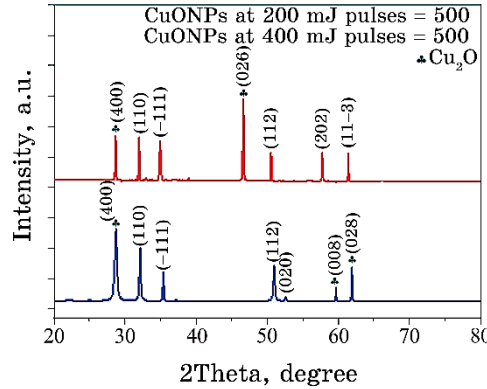


**Fig. 12.** XRD patterns of the samples prepared by laser ablation in DDW.

## 3.2. Morphology and Particle Size Analysis for CuO NPs

### 3.2.1. X-Ray Diffraction Patterns

The XRD patterns of CuO NPs in DDW laser-ablated at 200 mJ and 400 mJ with same number of pulses (500) are shown in Fig. 12. The average crystallite size was computed using the Debye–Scherrer equation [33]:

$$D_{av} = \frac{k\lambda_{x\text{-ray}}}{\beta \cos \theta}, \quad (3)$$

where the shape factor constant  $k$  is of 0.9,  $\lambda_{x\text{-ray}}$  the x-ray wavelength is of 0.15406 nm,  $\beta$  is the full width at half-maximum FWHM intensity in radians, and  $\theta$  is the diffraction angle (Bragg angle). The calculated average crystallite size for CuO nanoparticles is found to be between 50 nm and 73 nm for 200 mJ and 400 mJ, respectively. The analysis of x-ray diffraction patterns revealed that CuO NPs have the crystallographic planes of monoclinic (1 1 0), (1 1 0), (−1 1 1), (1 1 2), (0 2 0), (0 2 0) and (1 1 −3) can be indexed to the diffraction peaks at about  $2\theta = 32, 35, 51, 58$  and  $61^\circ$  conformed to the ICSD standard No. 98-004-3181; 01-089-2531. Furthermore, the diffraction peaks at around  $2\theta = 28, 46, 59$  and  $61^\circ$  can be assigned to the crystallographic planes (4 0 0), (0 2 6), (0 0 8), and (0 2 8) which can be regarded as an orthorhombic crystal system. This is consistent with the standard ICSD No. 98-008-5080. The XRD results also corroborate the absence of impurities in the ablated nanoparticles, as the XRD patterns do not contain any peaks other than CuO nanoparticles. Using Scherrer's equation, the mean crystallite size of each sample was determined.

As shown in Table, the mean crystallite size of laser-ablated nanoparticles increases marginally with increasing pulse energy, according to the literature [34, 35].

CuO nanoparticles may be formed by two common processes, the thermal evaporation of atomic (and ionic) species from the liquid–solid interface and the thermally-induced discharge of nanometer-size molten droplets from the target. At the interface of liquid and target, the adiabatic expansion of the created plasma confines the surrounding double distilled water. The presence of PLAL in DDW solution results in an oxygen-rich cavitation bubble environment. Plasma's high temperature and pressure create the chemical conditions for the formation of CuO. Therefore, species within the plasma plume can interact to produce CuO nanoparticles. Eventually, the plasma is extinguished, and the CuO structures solidify [36, 37]. In addition, DDW can react with molten particles, and molten Cu oxidation contributes to the formation of CuO. Consequently, both of these phenomena may be responsible for the formation of CuO structures [38, 39].

TABLE. X-ray diffraction of samples prepared.

(200 mJ, pulses = 500) CuO NPs						(400 mJ, pulses = 500) CuO NPs					
Exp. $2\theta$ , degree	FWHM, degree	$h\ k\ l$	Compound name	Crystallite size, nm		Exp. $2\theta$ , degree	FWHM, degree	$h\ k\ l$	Compound name	Crystallite size, nm	
28.728	0.492	4 0 0	CuO <sub>2</sub>	16.667		28.672	0.161	4 0 0	CuO <sub>2</sub>	50.929	
32.091	0.314	1 1 0	CuO	26.325		31.924	0.105	1 1 0	CuO	78.693	
35.397	0.136	-1 1 1	CuO	61.316		34.941	0.246	-1 1 1	CuO	33.855	
51.979	0.281	1 1 2	CuO	31.452		46.972	0.217	0 2 6	CuO <sub>2</sub>	39.916	
52.554	0.235	0 2 0	CuO	37.701		50.559	0.092	1 1 2	CuO	95.496	
59.679	0.103	0 0 8	CuO <sub>2</sub>	88.917		57.741	0.089	2 0 2	CuO	101.930	
61.902	0.105	0 2 8	CuO <sub>2</sub>	88.223		61.338	0.083	1 1 -3	CuO	111.279	
				Average crystallite size, nm						Average crystallite size, nm	
				50.8						73.1	

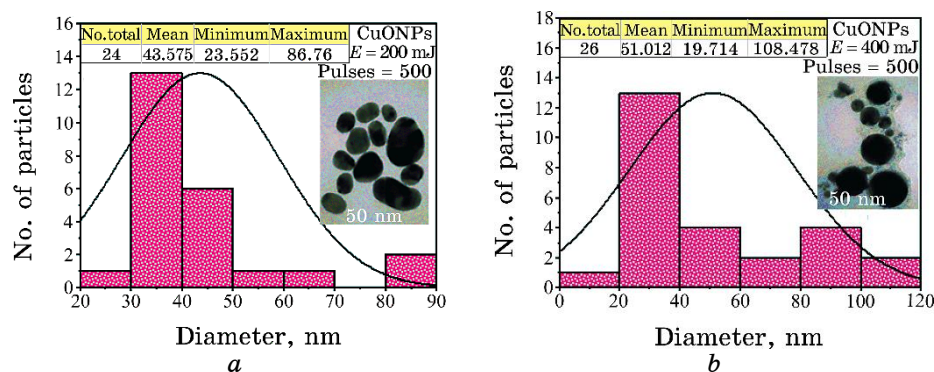


Fig. 13. TEM images and the particle size distribution of copper-oxide NPs with (a) 200 mJ (b) 400 mJ at 500 pulses.

### 3.2.2. Transmission Electron Microscopy (TEM)

Transmission EM analysis was used to confirm the average particle size, size distribution, and morphology of individual CuO nanoparticles prepared by the PLAL technique under 200 mJ and 400 mJ with 500 pulses. Analysis of TEM images uses the Image J program. The TEM image in Fig. 13 clearly shows that the aforementioned NPs have morphology, which is almost spherical. Copper oxide NPs diameters between 44 and 51 nm were confirmed by the TEM image. Using TEM analysis, which is consistent with that obtained from x-ray diffraction, On the other hand, because CuO nanoparticles tend to agglomerate, the agglomeration of nanoparticles can be attributed to the absence of antiagglomeration agents in the colloidal aqueous solution.

## 4. ANTIBACTERIAL ACTIVITY OF COPPER-OXIDE NPs

The diameter of inhibition zones was estimated using a meter ruler, and the mean value for each organism was recorded for two types of bacteria. The samples of CuO NPs with 500 pulses and laser energies of 200 mJ and 400 mJ were poured into wells on plates. DDW was used as a negative control to determine the antibacterial activity. According to our investigation, the CuO NPs produced did not significantly suppress the growth of the bacteria *S. aureus* G(+ve) and *E. coli* G(-ve). A surge in bacterial resistance may be to blame for this. Additionally, efficiency of nanoparticle synthesis by the PLAL technique is low compared with other synthesis techniques [34]. The copper-oxide NPs prepared by PLAL have inhibitory areas that can be seen in Figs. 14, 15 for both the energy and pulse con-



**Fig. 14.** Photograph of the antibacterial activity test of CuO NPs prepared for *Staphylococcus aureus* and *Escherichia coli*.

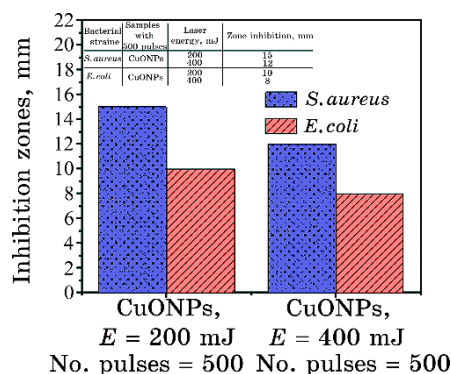


**Fig. 15.** Histogram of antibacterial activity for CuO NPs at 200 mJ and 400 mJ with the same number of 500 pulses.

figurations indicated. For the same number of pulses, the 200-mJ nanoparticles were more effective than the 400-mJ ones. In many instances, it is still unclear whether the death of the bacterium was caused by a single mechanism or a mixture of mechanisms. Negatively charged bacterial cell surfaces and positively charged nanoparticles may attract each other electrostatically. In contact with bacterial cells, copper oxide nanoparticles can pierce the cell wall and break the cell membrane, causing the release of cellular contents and ultimately cell death.

## 5. CONCLUSIONS

Copper-oxide nanoparticles can be easily produced by using the laser ablation technique on a copper target in double-distilled water. After several analyses were performed to investigate and characterize

the Cu NPs, according to UV-visible spectroscopy, the absorbance increased as the number of pulses increased. As the number of laser pulses increased, the plasmon peak at 217 nm redshifted. The compounds associated with the oxidation of Cu NPs into CuO NPs were produced by the reaction of dissolved oxygen in water with the Cu NPs. At the same number of pulses, copper-oxide NPs prepared at 400 mJ have a larger size than samples prepared at 200 mJ. CuO nanoparticles have a spherical shape and diameters ranging from 46 nm to 52 nm for 200 mJ and 400 mJ, respectively. However, compared to *Escherichia coli* (gram *-ve*) bacteria, the tested *Staphylococcus aureus* (gram *+ve*) bacteria demonstrated a higher sensitivity to copper-oxide NPs. This is due to variations in the molecular makeup of the cell walls of these bacterial strains. The results of our study show that when the laser energy is low and the same number of pulses, copper oxide nanoparticles have a stronger antibacterial effect against *S. aureus* and *E. coli*, respectively.

### ACKNOWLEDGEMENTS

The authors would like to express their warmest thanks to University of Mosul, College of Education for Pure Science, Department of Physics for supporting this work.

### REFERENCES

1. I. Khan, K. Saeed, and I. Khan, *Arabian Journal of Chemistry*, **12**, Iss. 7: 908 (2019); <https://doi.org/10.1016/j.arabjc.2017.05.011>
2. A. Abedini, A. A. Bakar, F. Larki, P. S. Menon, M. S. Islam, and S. Shaari, *Nanoscale Research Letters*, **11**: 1 (2016); <https://doi.org/10.1186/s11671-016-1500-z>
3. D. Zhang, B. Gökçe, and S. Barcikowski, *Chemical Reviews*, **117**, No. 5: 3990 (2017); <https://doi.org/10.1021/acs.chemrev.6b00468>
4. S. M. Arakelyan, V. P. Veiko, S. V. Kutrovsкая, A. O. Kucherik, A. V. Osipov, T. A. Vartanyan, and T. E. Itina, *Journal of Nanoparticle Research*, **18**, Iss. 6: 1 (2016); <https://doi.org/10.1007/s11051-016-3468-0>
5. T. T. P. Nguyen, R. Tanabe, and Y. Ito, *Optics & Laser Technology*, **100**: 21 (2018); <https://doi.org/10.1016/j.optlastec.2017.09.021>
6. T. T. P. Nguyen, R. Tanabe, and Y. Ito, *Applied Physics A*, **116**: 1109 (2013); <https://doi.org/10.1007/s00339-013-8193-2>
7. I. Akhatov, O. Lindau, A. Topolnikov, R. Mettin, N. Vakhitova, and W. Lauterborn, *Physics of Fluids*, **13**, Iss. 10: 2805 (2001); <https://doi.org/10.1063/1.1401810>
8. S. Ibrahimkutty, P. Wagener, A. Menzel, A. Plech, and S. Barcikowski, *Applied Physics Letters*, **101**, Iss. 10: 103104 (2012); <https://doi.org/10.1063/1.4750250>
9. I. Akhatov, N. Vakhitova, A. Topolnikov, K. Zakirov, B. Wolfrum, T. Kurz,

- O. Lindau, R. Mettin, and W. Lauterborn, *Experimental Thermal and Fluid Science*, **26**, Iss. 6–7: 731 (2002); [https://doi.org/10.1016/S0894-1777\(02\)00182-6](https://doi.org/10.1016/S0894-1777(02)00182-6)
10. A. Letzel, B. Gökce, P. Wagener, S. Ibrahimkutty, A. Menzel, A. Plech, and S. Barcikowski, *The Journal of Physical Chemistry C*, **121**: 5356 (2017); <https://doi.org/10.1021/acs.jpcc.6b12554>
  11. M. Q. Jiang, X. Q. Wu, Y. P. Wei, G. Wilde, and L. H. Dai, *Extreme Mechanics Letters*, **11**: 24 (2017); <https://doi.org/10.1016/j.eml.2016.11.014>
  12. H. Zeng, X. Du, S. C. Singh, S. A. Kulinich, S. Yang, J. He, and W. Cai, *Advanced Functional Materials*, **22**, Iss. 7: 1333 (2012); <https://doi.org/10.1002/adfm.201102295>
  13. J. Xiao, P. Liu, C. X. Wang, and G. W. Yang, *Progress in Materials Science*, **87**: 140 (2017); <https://doi.org/10.1016/j.pmatsci.2017.02.004>
  14. S. Bashir, M. S. Rafique, C. S. Nathala, and W. Husinsky, *Applied Surface Science*, **290**: 53 (2014); <https://doi.org/10.1016/j.apsusc.2013.10.187>
  15. M. Curcio, A. De Bonis, A. Santagata, A. Galasso, and R. Teghil, *Optics & Laser Technology*, **138**: 106916 (2021); <https://doi.org/10.1016/j.optlastec.2021.106916>
  16. A. Baladi and R. S. Mamoory, *Applied Surface Science*, **256**, Iss. 24: 7559 (2010); <https://doi.org/10.1016/j.apsusc.2010.05.103>
  17. S. A. Al-Mamun, R. Nakajima, and T. Ishigaki, *Journal of Colloid and Interface Science*, **392**: 172 (2013); <https://doi.org/10.1016/j.jcis.2012.10.027>
  18. S. Besner, A. V. Kabashin, and M. Meunier, *Applied Physics A*, **88**, No. 2: 269 (2007); <https://doi.org/10.1007/s00339-007-4001-1>
  19. G. W. Yang, *Progress in Materials Science*, **52**, Iss. 4: 648 (2007); <https://doi.org/10.1016/j.pmatsci.2006.10.016>
  20. R. C. Ashoori, *Nature*, **379**: 413 (1996); <https://doi.org/10.1038/379413a0>
  21. A. P. Alivisatos, *Science*, **271**, Iss. 5251: 933 (1996); <https://doi.org/10.1126/science.271.5251.933>
  22. A. S. Zoolfakar, R. A. Rani, A. J. Morfa, A. P. O'Mullane, and K. Kalantar-Zadeh, *Journal of Materials Chemistry C*, **2**, Iss. 27: 5247 (2014); <https://doi.org/10.1039/C4TC00345D>
  23. H. Azadi, H. D. Aghdam, R. Malekfar, and S. M. Bellah, *Results in Physics*, **15**: 102610 (2019); <https://doi.org/10.1016/j.rinp.2019.102610>
  24. J. Prikulis, F. Svedberg, M. Käll, J. Enger, K. Ramser, M. Goksör, and D. Hanstorp, *Nano Letters*, **4**, No. 1: 115 (2004); <https://doi.org/10.1021/nl0349606>
  25. A. Azam, A. S. Ahmed, M. Oves, M. S. Khan, and A. Memic, *International Journal of Nanomedicine*, **7**: 3527 (2012); <http://dx.doi.org/10.2147/IJN.S29020>
  26. A. F. Halbus, T. S. Horozov, and V. N. Paunov, *ACS Applied Materials & Interfaces*, **11**, No. 13: 12232 (2019); <https://doi.org/10.1021/acsami.8b21862>
  27. J. Tauc, R. Grigorvici, and A. Vancu, *physica status solidi (b)*, **15**, Iss. 2: 627 (1966); <https://doi.org/10.1002/pssb.19660150224>
  28. Triloki, R. Rai, and B. K. Singh, *Nuclear Instruments and Methods in Physics Research Section A: Accelerators, Spectrometers, Detectors and Associated Equipment*, **785**: 70 (2013); <http://dx.doi.org/10.1016/j.nima.2015.02.059>

29. M. D. Migahed and H. M. Zidan, *Current Applied Physics*, **6**, Iss. 1: 91 (2006); <https://doi:10.1016/j.cap.2004.12.009>
30. I. Saini, J. Rozra, N. Chandak, S. Aggarwal, P. K. Sharma, and A. Sharma, *Materials Chemistry and Physics*, **139**, Iss. 2–3: 802 (2013); <https://doi:10.1016/j.matchemphys.2013.02.035>
31. D. Babu, P. Philominathan, and K. Murali, *Optik*, **186**: 350 (2019); <https://doi.org/10.1016/j.ijleo.2019.03.048>
32. V. R. Kumar, P. R. S. Wariar, and J. Koshy, *Crystal Research and Technology*, **45**, Iss. 6: 619 (2010); <https://doi.org/10.1002/crat.201000048>
33. A. A. Menazea, *Radiation Physics and Chemistry*, **168**: 108616 (2020); <https://doi.org/10.1016/j.radphyschem.2019.108616>
34. *Laser Ablation in Liquids: Principles and Applications in the Preparation of Nanomaterials* (Ed. G. Yang) (New York: Jenny Stanford Publishing: 2012); <https://doi.org/10.1201/b11623>
35. J. Zhang, J. Claverie, M. Chaker, and D. Ma, *Chem. Phys. Chem.*, **18**, Iss. 9: 986 (2017); <https://doi.org/10.1002/cphc.201601220>
36. H. Zeng, W. Cai, Y. Li, J. Hu, and P. Liu, *The Journal of Physical Chemistry B*, **109**, No. 39: 18260 (2005); <https://doi.org/10.1021/jp052258n>
37. H. Zeng, X. Xu, Y. Bando, U. K. Gautam, T. Zhai, X. Fang, B. Liu, and D. Golberg, *Advanced Functional Materials*, **19**, Iss. 19: 3165(2009); <https://doi.org/10.1002/adfm.200900714>
38. K. Y. Niu, J. Yang, S. A. Kulinich, J. Sun, H. Li, and X. W. Du, *Journal of the American Chemical Society*, **132**, No. 28: 9814 (2010); <https://doi.org/10.1021/ja102967a>
39. M. A. Gondal, T. F. Qahtan, M. A. Dastageer, T. A. Saleh, Y. W. Maganda, and D. H. Anjum, *Applied Surface Science*, **286**: 149 (2013); <https://doi.org/10.1016/j.apsusc.2013.09.038>